INSTITUTE OF PHYSICS PUBLISHING INVERSE PROBLEMS

Inverse Problems **17** (2001) 1671–1688 PII: S0266-5611(01)24165-3

Modified[2] gradient method and modified Born method for solving a two-dimensional inverse scattering problem

Kamal Belkebir[1,3] **and Anton G Tijhuis**[2]

[1] Institut Fresnel, UMR-CNRS 6133, Campus de Saint Jérôme, case 162, 13397 Marseille Cedex 20, France
[2] Faculty of Electrical Engineering, Eindhoven University of Technology, PO Box 513, 5600 MB Eindhoven, The Netherlands

E-mail: kamal.belkebir@fresnel.fr

Received 23 April 2001, in final form 10 September 2001
Published 13 November 2001
Online at stacks.iop.org/IP/17/1671

Abstract

This paper concerns the reconstruction of the complex relative permittivity of an inhomogeneous object from the measured scattered field. The parameter of interest is retrieved using iterative techniques. Four methods are considered, in which the permittivity is updated along the standard Polak–Ribière conjugate gradient directions of a cost functional. The difference lies in the update direction for the field, and the determination of the expansion coefficients. In the modified gradient method, the search direction is the conjugate gradient direction for the field, and the expansion coefficients for field and profile are determined simultaneously. In the Born method (BM) the field is considered as the fixed solution of the forward problem with the available estimate of the unknown permittivity, and only the profile coefficients are determined from the cost function. In the modified Born method, we use the same field direction as in the BM, but determine the coefficients for field and profile simultaneously. In the modified[2] gradient method, we use both field directions, and again update all coefficients simultaneously. Examples of the reconstruction of either metal or dielectric cylinders from experimental data are presented and the methods are compared for a range of frequencies.

1. Introduction

The aim of the electromagnetic inverse scattering problem is to determine properties, (e.g. position, shape and the constitutive material) of unknown objects, from their response (scattered field) to a known electromagnetic excitation. We restrict our study to iterative

[3] To whom correspondence should be addressed.

techniques for solving such inverse scattering problems. In these methods, starting from an initial guess, the parameter of interest is adjusted gradually by minimizing a cost function involving the measured scattered field data. A brief review of the literature shows two approaches, depending on whether the field in the scattering domain is considered as fixed (solution of the direct problem for the best available estimation of the parameter) in each iteration step [1, 2] or as an unknown that is obtained together with the parameter by the minimization procedure [3, 4]. We present herein one method from each category, and two 'hybrid' ones, which combine ideas from the first two methods. Some details on the most advanced 'hybrid' method, referred to from now on as modified^2 gradient method (M2GM), can be found in [5]. In that paper, a comparison between M2GM and a method that alternatively retrieves the boundaries and the constitutive material of homogeneous objects [6] is presented. We herein focus on M2GM and compare the method to the standard modified gradient method (MGM) as well as to a new Born-type iterative method (BM) and the modified Born method (MBM). We report and compare results of reconstruction of dielectric or conducting objects from experimental data with the aid of the iterative techniques mentioned above. We refer the reader to a similar work [7] comparing different methods including some which are presented in this paper, particularly the MGM.

2. Notations and statement of the problem

The geometry of the problem studied in this paper is shown in figure 1 where a two-dimensional object of arbitrary cross-section Ω_o is confined in a bounded domain Ω. The embedding medium Ω_b is assumed to be infinite and homogeneous, with permittivity $\varepsilon_b = \varepsilon_0\varepsilon_{br}$, and of permeability $\mu = \mu_0$ (ε_0 and μ_0 being the permittivity and permeability of the vacuum, respectively). The scatterers are assumed to be inhomogeneous dielectric cylinders with complex permittivity distribution $\varepsilon(\boldsymbol{r}) = \varepsilon_0\varepsilon_r(\boldsymbol{r})$; the entire configuration is non-magnetic ($\mu = \mu_0$).

A right-handed Cartesian coordinate frame (O, $\boldsymbol{u}_x$, $\boldsymbol{u}_y$, $\boldsymbol{u}_z$) is defined. The origin O can be either inside or outside the scatterer and the z-axis is parallel to the invariance axis of the scatterer. The position vector $\boldsymbol{OM}$ can then be written as

$$\boldsymbol{OM} = x\,\boldsymbol{u}_x + y\,\boldsymbol{u}_y + z\,\boldsymbol{u}_z = \boldsymbol{r} + z\,\boldsymbol{u}_z. \tag{1}$$

The sources that generate the electromagnetic excitation are assumed to be lines parallel to the z-axis, located at $(\boldsymbol{r}_l)_{1\leqslant l\leqslant L}$. Taking into account a time factor $\exp(-\mathrm{i}\omega t)$, in the TM case the time-harmonic incident electric field created by the lth line source is given by

$$\boldsymbol{E}_l^{\mathrm{inc}}(\boldsymbol{r}) = E_l^{\mathrm{inc}}(\boldsymbol{r})\boldsymbol{u}_z = P\frac{\omega\mu_0}{4}H_0^{(1)}(k_b\,|\boldsymbol{r}-\boldsymbol{r}_l|)\,\boldsymbol{u}_z, \tag{2}$$

where P is the strength of the electric source, ω the angular frequency, $H_0^{(1)}$ the Hankel function of zero order and of the first kind and k_b the wavenumber in the surrounding medium.

For the inverse scattering problem we assume that the unknown object is successively illuminated by L electromagnetic excitations and for each incident field the scattered field is available along a contour Γ at M positions. For each excitation, the direct scattering problem may be reformulated as two coupled contrast-source integral relations: the state or observation equation (3) and the field or coupling equation (4)

$$E_l^d(\boldsymbol{r}\in\Gamma) = k_0^2\int_\Omega \chi(\boldsymbol{r}')\,E_l(\boldsymbol{r}')\,G(\boldsymbol{r},\boldsymbol{r}')\,\mathrm{d}\boldsymbol{r}', \tag{3}$$

$$E_l(\boldsymbol{r}\in\Omega) = E_l^{\mathrm{inc}} + k_0^2\int_\Omega \chi(\boldsymbol{r}')\,E_l(\boldsymbol{r}')\,G(\boldsymbol{r},\boldsymbol{r}')\,\mathrm{d}\boldsymbol{r}', \tag{4}$$

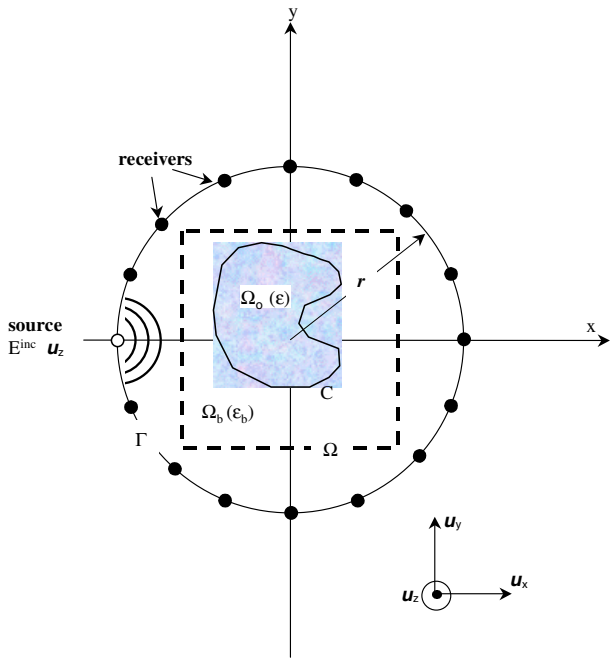

Figure 1. Geometry of the problem.

where $\chi(\boldsymbol{r}) = \varepsilon_r(\boldsymbol{r}) - \varepsilon_{br}$ denotes the permittivity contrast which vanishes outside $\Omega \supset \Omega_o$, $G(\boldsymbol{r}, \boldsymbol{r}')$ is the two-dimensional homogeneous free space Green function and k_0 represents the wavenumber in the vacuum. For the sake of simplicity, equations (3) and (4) are rewritten in operator notation as

$$E_l^d = \boldsymbol{G}_\Gamma \, \chi \, E_l, \tag{5}$$

$$E_l = E_l^{\text{inc}} + \boldsymbol{G}_\Omega \, \chi \, E_l. \tag{6}$$

3. Principles of the inversion algorithms

The inverse scattering problem consists now in finding the function $\chi(\boldsymbol{r} \in \Omega)$ in the investigated area Ω (test domain) so that the diffracted field associated to χ matches the measured diffracted field $f_l(\boldsymbol{r} \in \Gamma)$.

3.1. Modified gradient method

The basic idea underlying the MGM [3, 9] for solving this inverse scattering problem is to build up two sequences related to contrast and total field $\{\chi_n\}$ and $\{E_{l,n}\}$, respectively, inside the test domain according to the following recursive relations:

$$E_{l,n} = E_{l,n-1} + \alpha_{l,n} v_{l,n}, \tag{7}$$

$$\chi_n = \chi_{n-1} + \beta_n d_n, \tag{8}$$

where $v_{l,n}$ and d_n are search directions with respect to the total field $E_{l,n}$ and to the contrast, respectively. The choice of these search directions will be discussed in the next section. The scalar coefficients $\{\alpha_{l,n}\}$ and $\{\beta_n\}$ are weights that are chosen at each iteration step n such that

they minimize the normalized cost functional $\mathcal{F}_n(\chi_n, E_{l,n})$ given by

$$\mathcal{F}_n(\chi_n, E_{l,n}) = W_\Omega \sum_{l=1}^{L} \| h_{l,n}^{(1)} \|_\Omega^2 + W_\Gamma \sum_{l=1}^{L} \| h_{l,n}^{(2)} \|_\Gamma^2, \tag{9}$$

where the normalizing coefficients W_Ω and W_Γ are defined as

$$W_\Omega = \frac{1}{\sum_{l=1}^{L} \| E_l^{\mathrm{inc}} \|_\Omega^2}, \qquad W_\Gamma = \frac{1}{\sum_{l=1}^{L} \| f_l \|_\Gamma^2}. \tag{10}$$

The subscripts Ω and Γ are included in the norm $\| \cdot \|$ and later in the inner product $\langle \cdot, \cdot \rangle$ to indicate the domain of integration. The functions $h_{l,n}^{(1)}$ and $h_{l,n}^{(2)}$ are two residual errors defined as

$$h_{l,n}^{(1)} = E_l^{\mathrm{inc}} - E_{l,n-1} + \boldsymbol{G}_\Omega \chi_n E_{l,n}, \tag{11}$$

$$h_{l,n}^{(2)} = f_l - \boldsymbol{G}_\Gamma \chi_n E_{l,n}. \tag{12}$$

The use of *a priori* information may improve the effectiveness of the inversion algorithm. For instance in [8] a binary constraint is used to reconstruct the shape of homogeneous objects with known constitutive parameters and in [9] non-negative *a priori* information is applied to a pure imaginary contrasted object (conducting object). In [10] non-negative *a priori* information is used to retrieve the shape of homogeneous objects. Here we incorporated *a priori* information stating that both real and imaginary parts of the susceptibility ζ are non-negative ($\varepsilon_r(\boldsymbol{r}) = 1 + \zeta(\boldsymbol{r})$). Instead of retrieving a complex function χ_n, two real auxiliary functions ξ_n and η_n are reconstructed such that

$$\chi_n = 1 + \xi_n^2 + \mathrm{i}\eta_n^2 - \varepsilon_{br}, \tag{13}$$

wherein the real and imaginary parts of the relative complex permittivity distribution are forced to be greater than unity and non-negative, respectively ($\mathrm{Re}\,[\varepsilon_r(\boldsymbol{r})] \geqslant 1$; $\mathrm{Im}\,[\varepsilon_r(\boldsymbol{r})] \geqslant 0$; $\forall \boldsymbol{r} \in \Omega$). The recursive relation with respect to the complex contrast function χ_n (equation (8)) is refined as

$$\xi_n = \xi_{n-1} + \beta_{n;\xi} d_{n;\xi}, \tag{14}$$

$$\eta_n = \eta_{n-1} + \beta_{n;\eta} d_{n;\eta}, \tag{15}$$

where all quantities are real. Once the updating directions $d_{n;\xi}$, $d_{n;\eta}$ and $v_{l,n}$ are found, $\mathcal{F}_n$ is a nonlinear expression with L complex variables $\{\alpha_{l,n;v}\}$ and two real variables $\{\beta_{n;\xi}, \beta_{n;\eta}\}$. The minimization of $\mathcal{F}_n$ is accomplished using the Polak–Ribière conjugate gradient procedure [11].

3.1.1. Search directions. As updating directions $d_{n;\xi}$ and $d_{n;\eta}$, the authors took the standard Polak–Ribière conjugate gradient directions [9, 10]

$$d_{n;\xi} = g_{n;\xi} + \gamma_{n;\xi} d_{n-1;\xi} \qquad \gamma_{n;\xi} = \frac{\langle g_{n;\xi}, g_{n;\xi} - g_{n-1;\xi} \rangle_\Omega}{\| g_{n-1;\xi} \|_\Omega^2}, \tag{16}$$

$$d_{n;\eta} = g_{n;\eta} + \gamma_{n;\eta} d_{n-1;\eta} \qquad \gamma_{n;\eta} = \frac{\langle g_{n;\eta}, g_{n;\eta} - g_{n-1;\eta} \rangle_\Omega}{\| g_{n-1;\eta} \|_\Omega^2}, \tag{17}$$

where g_ξ and g_η are the gradients of the cost functional $\mathcal{F}_n(\xi, \eta, E_l)$ with respect to ξ and η respectively, evaluated at the $(n-1)$th step assuming that the total field inside the test domain does not change. These gradients are given by

$$g_{n;\xi} = 2\xi_{n-1} \mathrm{Re} \left[W_\Omega \sum_{l=1}^{L} \bar{E}_{l,n-1} \boldsymbol{G}_\Omega^\dagger h_{l,n-1}^{(1)} - W_\Gamma \sum_{l=1}^{L} \bar{E}_{l,n-1} \boldsymbol{G}_\Gamma^\dagger h_{l,n-1}^{(2)} \right], \tag{18}$$

$$g_{n;\eta} = 2\eta_{n-1} \mathrm{Im} \left[W_\Omega \sum_{l=1}^{L} \bar{E}_{l,n-1} \boldsymbol{G}_\Omega^\dagger h_{l,n-1}^{(1)} - W_\Gamma \sum_{l=1}^{L} \bar{E}_{l,n-1} \boldsymbol{G}_\Gamma^\dagger h_{l,n-1}^{(2)} \right], \tag{19}$$

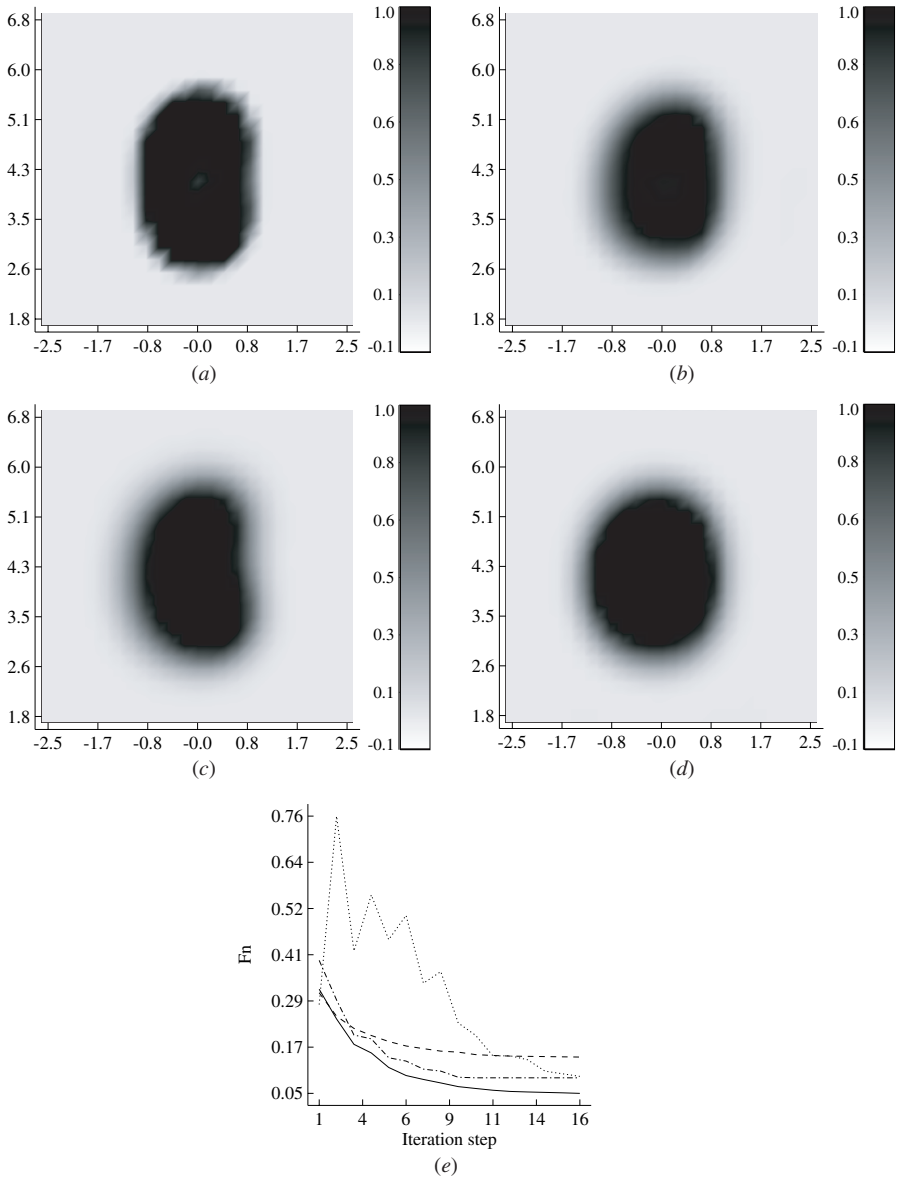

Figure 2. Reconstructed conductivity distribution of the rectangular metallic target at $f = 4$ GHz. (*a*) M2GM; (*b*) MGM; (*c*) MBM; (*d*) BM; (*e*) evolution of the cost function F_n as a function of iteration (——, M2GM; – – –, MGM; — · —, MBM; · · · · · ·, BM). Black in the images represents $\sigma\ [S\,m^{-1}] \geqslant 1$. The maximum value of the reconstructed conductivity is $\sigma = 6.8$, 1.3, 1.9 and 2.2 S m^{-1} for M2GM, MGM, MBM and MB, respectively. Other parameters are specified in the text.

where the overbar denotes the complex conjugate, and $\boldsymbol{G}_\Omega^\dagger$ and $\boldsymbol{G}_\Gamma^\dagger$ are the adjoint operators of $\boldsymbol{G}_\Omega$ and $\boldsymbol{G}_\Gamma$, respectively.

The search direction $v_{l,n}$ for the total field inside the test domain is similar to those chosen

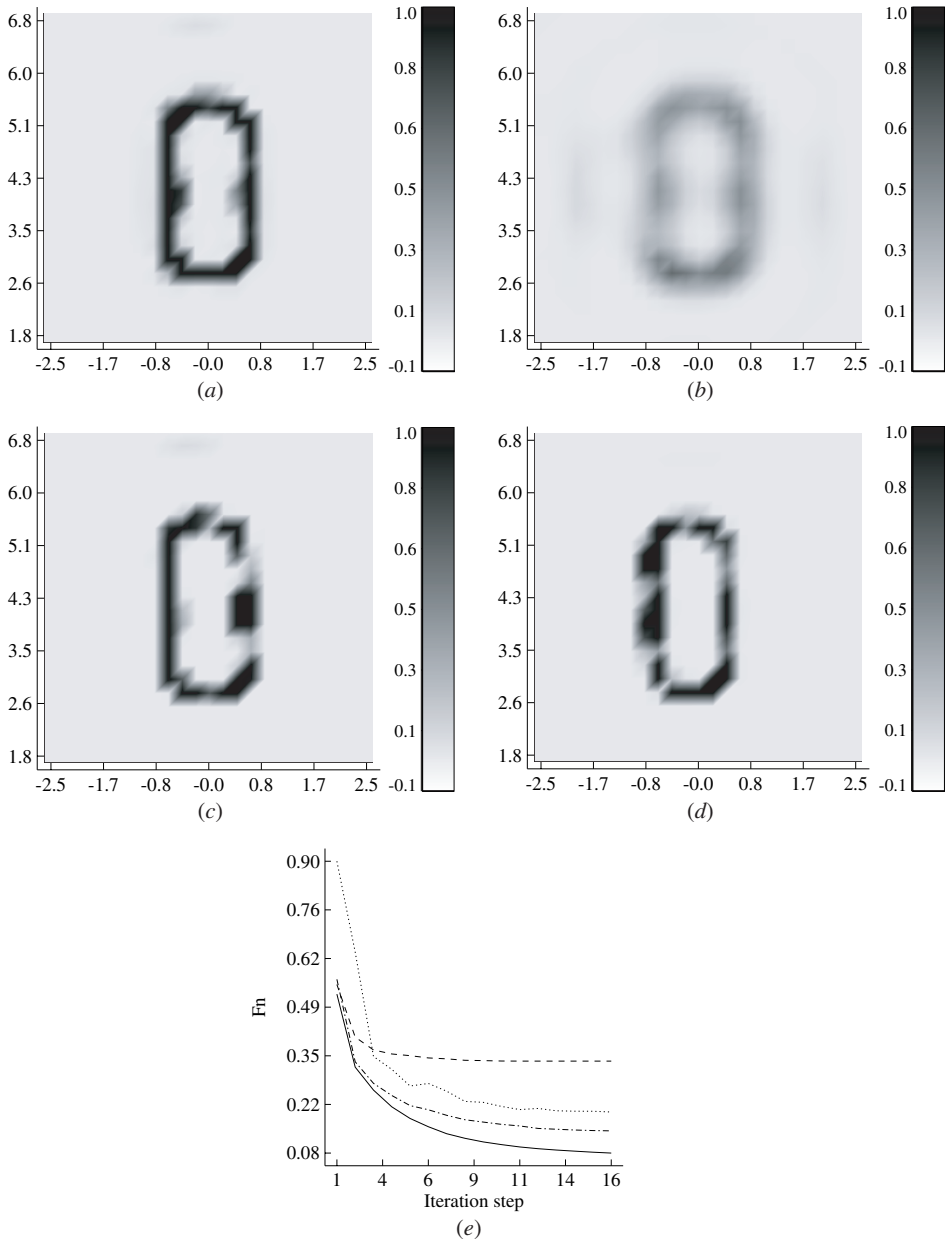

Figure 3. Reconstructed conductivity distribution of the rectangular metallic target at $f = 16$ GHz. (*a*) M2GM; (*b*) MGM; (*c*) MBM; (*d*) BM; (*e*) evolution of the cost function F_n as a function of iteration (——, M2GM; – – –, MGM; — · —, MBM; · · · · · ·, BM). Black in the images represents σ [S m^{-1}] $\geqslant 1$. The maximum value of the reconstructed conductivity is $\sigma = 5.8$, 0.6, 9.7 and 15.9 S m^{-1} for M2GM, MGM, MBM and MB, respectively. Other parameters are specified in the text.

for the object functions ξ and η:

$$v_{l,n} = g_{l,n;E} + \gamma_{l,n;E_l} v_{l,n-1} \qquad \gamma_{l,n;E_l} = \frac{\langle g_{l,n;E_l}, g_{l,n;E_l} - g_{l,n-1;E_l} \rangle_\Omega}{\| g_{l,n-1;E_l} \|^2_\Omega} \tag{20}$$

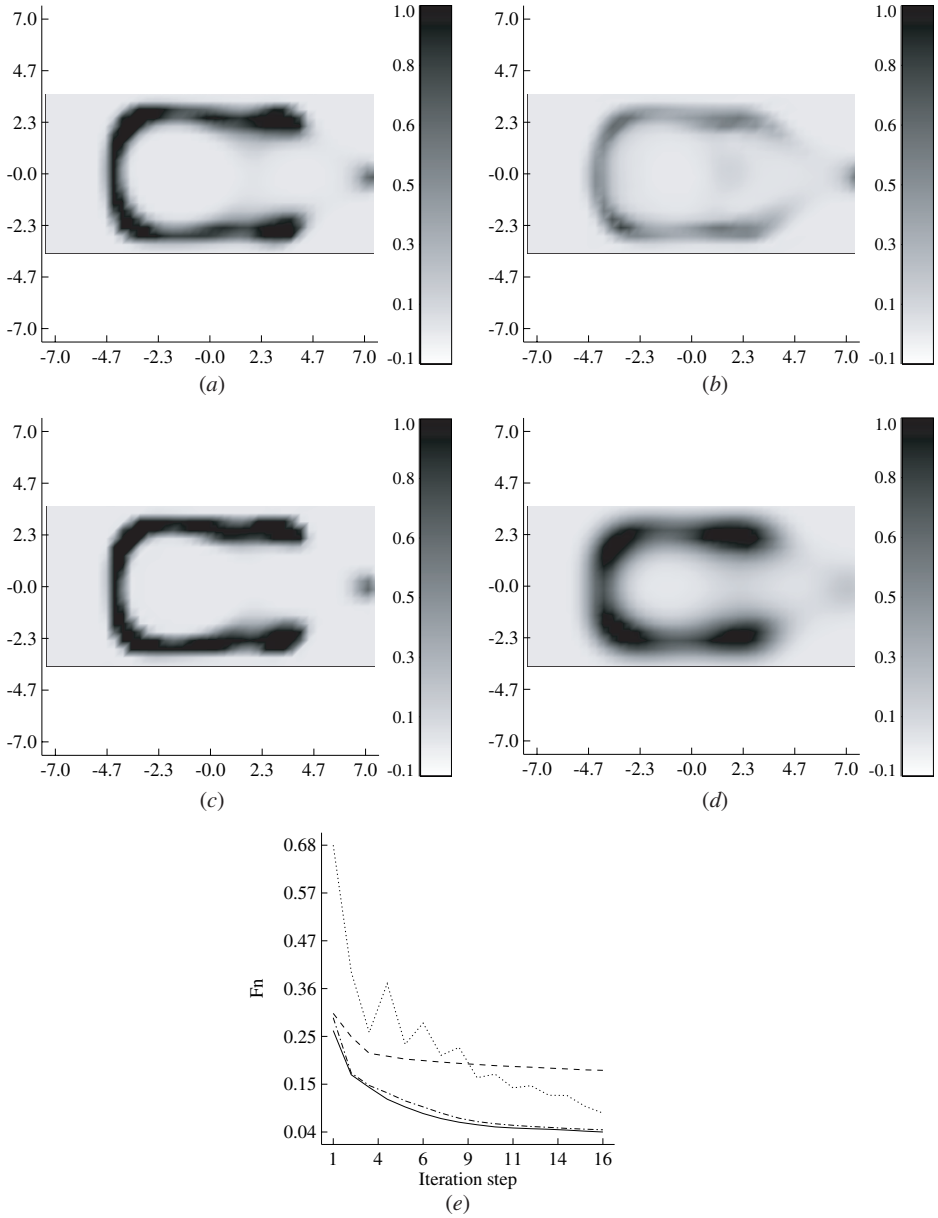

Figure 4. Reconstructed conductivity distribution of the 'U-shaped' metallic cylinder at $f = 4$ GHz. (*a*) M2GM; (*b*) MGM; (*c*) MBM; (*d*) BM; (*e*) cost function F_n as a function of iteration (——, M2GM; – – –, MGM; — · —, MBM; · · · · · ·, BM). Black in the images represents σ [S m^{-1}] $\geqslant 1$. The maximum value of the reconstructed conductivity is $\sigma = 2$, 0.8, 4.3 and 1.4 S m^{-1} for M2GM, MGM, MBM and BM, respectively. Other parameters are specified in the text.

where $g_{l,n;E_l}$ is the gradient of the cost functional $\mathcal{F}_n(\xi, \eta, E_l)$ with respect to the field E_l, evaluated at the $(n-1)$th step and assuming that ξ and η do not change:

$$g_{l,n;E_l} = W_\Omega[\bar{\chi}_{n-1}\boldsymbol{G}_\Omega^\dagger h_{l,n-1}^{(1)} - h_{l,n-1}^{(1)}] - W_\Gamma \bar{\chi}_l \boldsymbol{G}_\Gamma^\dagger h_{l,n-1}^{(2)}. \tag{21}$$

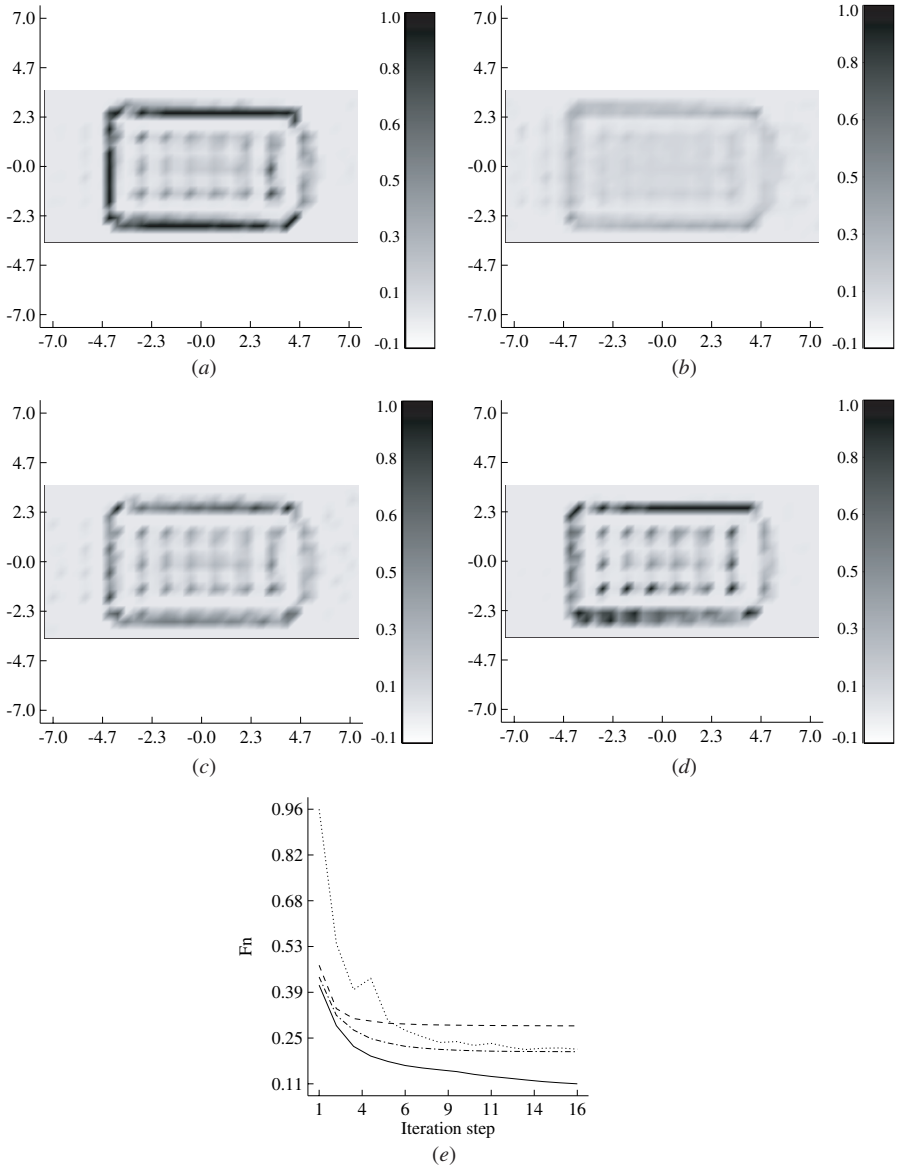

Figure 5. Reconstructed conductivity distribution of the 'U-shaped' metallic cylinder at $f = 16$ GHz. (*a*) M2GM; (*b*) MGM; (*c*) MBM; (*d*) BM; (*e*) cost function F_n as a function of iteration (——, M2GM; – – –, MGM; — · —, MBM; · · · · · ·, BM). Black in the images represents σ [S m^{-1}] $\geqslant 1$. The maximum value of the reconstructed conductivity is $\sigma = 2.2$, 0.3, 1.3 and 2.5 S m^{-1} for M2GM, MGM, MBM and BM, respectively. Other parameters are specified in the text.

3.2. Born and modified Born methods

In the Born method, for each iteration step n, the field $\tilde{E}_{l-1,n}$ inside the test domain Ω is given by

$$\tilde{E}_{l,n-1} = [1 - \boldsymbol{G}_\Omega \boldsymbol{\chi}_{n-1}]^{-1} E_l^{\text{inc}}, \tag{22}$$

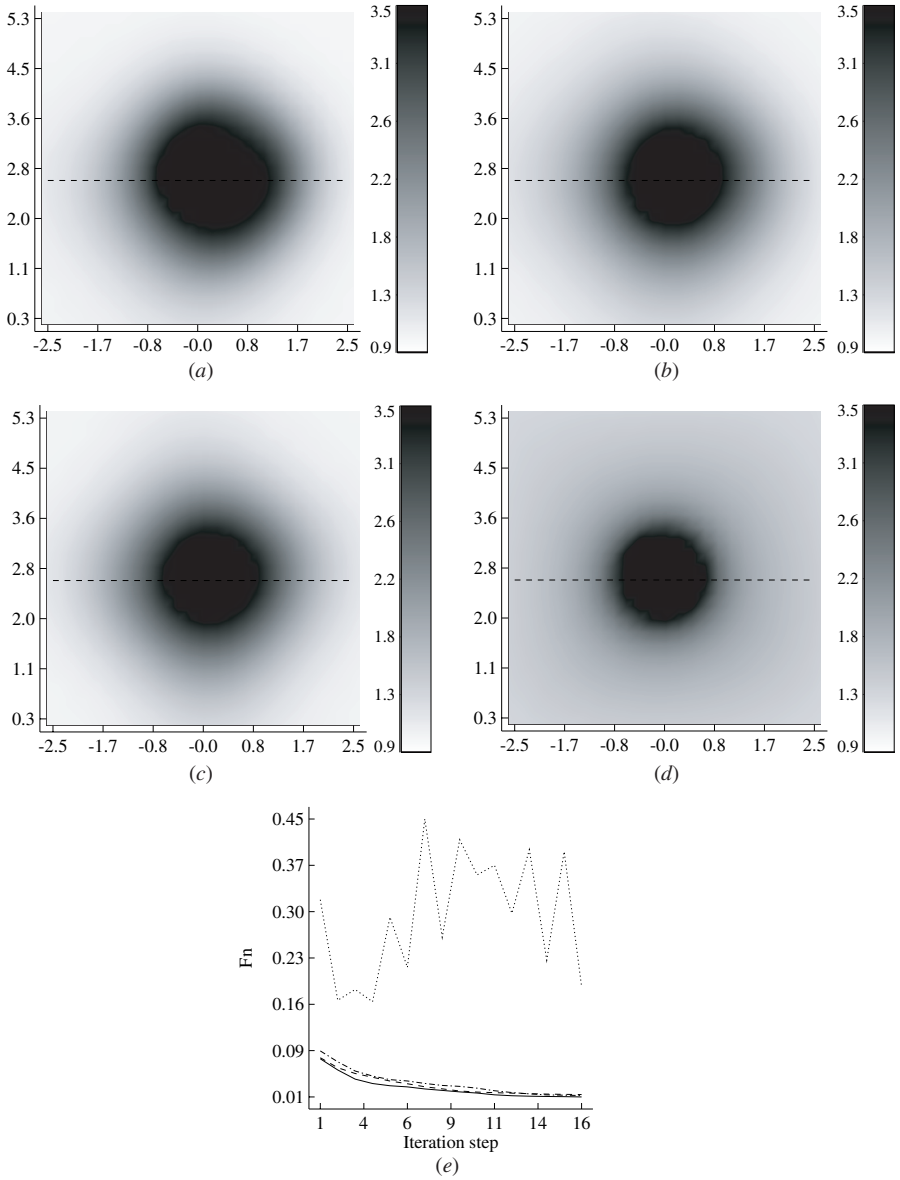

Figure 6. Reconstructed real part of the complex permittivity distribution of the circular dielectric cylinders at $f = 4$ GHz. (*a*) M2GM; (*b*) MGM; (*c*) MBM; (*d*) BM; (*e*) cost function F_n as a function of iteration (——, M2GM; – – –, MGM; — · —, MBM; · · · · · ·, BM). Black in the images represents $\varepsilon_r[\cdot] \geqslant 3.5$. Other parameters are specified in the text.

i.e. the field that would be present in domain Ω for contrast χ_{n-1}. This field is computed from the field equation (4) by generalizing the fast solution described in [12] to marching in angle and/or contrast. χ_n is improved along the conjugate gradient directions as specified in (16) and (17). The value of the coefficients $\{\gamma_{n;\xi}\}$ and $\{\gamma_{n;\eta}\}$ is obtained by minimizing the cost function $\mathcal{F}_n(\chi_n)$ defined in equation (9). In this computation, the field is fixed at $\tilde{E}_{l,n-1}$.

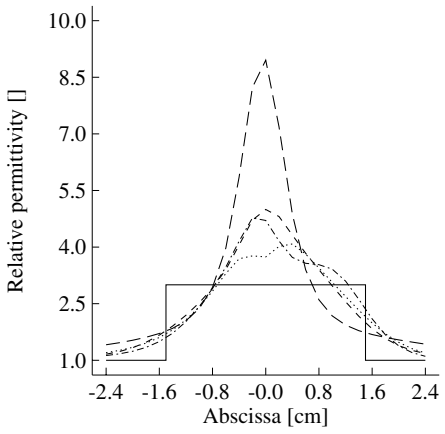

Figure 7. Comparison between the reconstructed profile and the actual one along the diameter plotted in dashed curve in the images of figure 6: ——, actual profile; — · —, M2GM; · · · · · ·, MGM; – – –, MBM; — — —, MB.

In the MBM, we update the field according to

$$E_{l,n} = E_{l,n-1} + \alpha_{l,n;w} w_{l,n}; \qquad w_{l,n} = \tilde{E}_{l,n-1} - E_{l,n-1}, \tag{23}$$

where the scalar coefficients $\{\alpha_{l,n;w}\}$ are determined jointly with the coefficients $\{\gamma_{n;\xi}\}$ and $\{\gamma_{n;\eta}\}$ by minimizing the cost function $\mathcal{F}_n(\chi_n, \alpha_{l,n;w})$. In this manner, we preserve the search direction from the BM, but with a guaranteed improvement of the value of the cost function.

3.3. Modified^2 gradient method

Since a fast forward solver is available for the present configuration [12], we modified the MGM by adding a second updating direction $w_{l,n}$ (defined in equation (23)) for the field $E_{l,n}$ such that the recursive relation (7) takes the following form:

$$E_{l,n} = E_{l,n-1} + \alpha_{l,n;v} v_{l,n} + \alpha_{l,n;w} w_{l,n}. \tag{24}$$

The cost function $\mathcal{F}_n$ is now a nonlinear expression with $2L$ complex variables $(\alpha_{l,n;v}, \alpha_{l,n;w})$ and two real variables $(\beta_{n;\xi}, \beta_{n;\eta})$. The minimization of $\mathcal{F}_n$ is again accomplished using the Polak–Ribière conjugate gradient method [11].

Note that if $\alpha_{l,n;v} = 0$ and $\alpha_{l,n;w} = 1$ then $E_{l,n} = \tilde{E}_{l,n-1}$. In this case the scheme is equivalent to the BM. If $\alpha_{l,n;v} = 0$ and $\alpha_{l,n;w}$ is arbitrary, then $E_{l,n} = E_{l,n-1} + \alpha_{l,n;v} w_{l,n}$, which amounts to the MBM. Choosing ($\alpha_{l,n;v} \neq 0$ and $\alpha_{l,n;w} = 0$) results in $E_{l,n} = E_{l,n-1} + \alpha_{l,n;v} v_{l,n}$, which provides us with the standard MGM. Therefore, the algorithm presented above can be considered as a hybrid one combining MGM and BM. This identification also makes it easy to switch between methods.

3.4. Initial estimates

Given the *a priori* information stating that the object functions ξ and η are positive, the initial guess ($\xi_0 = \eta_0 = 0$) must be rejected since it involves vanishing gradients ($g_{1;\xi} = g_{1;\eta} = 0$). This is caused by the circumstance that the transformation (13) introduces a local maximum of the cost function. We therefore need another initial guess. This can be provided by the backpropagation method. Details and additional references on the backpropagation method can be found in [5].

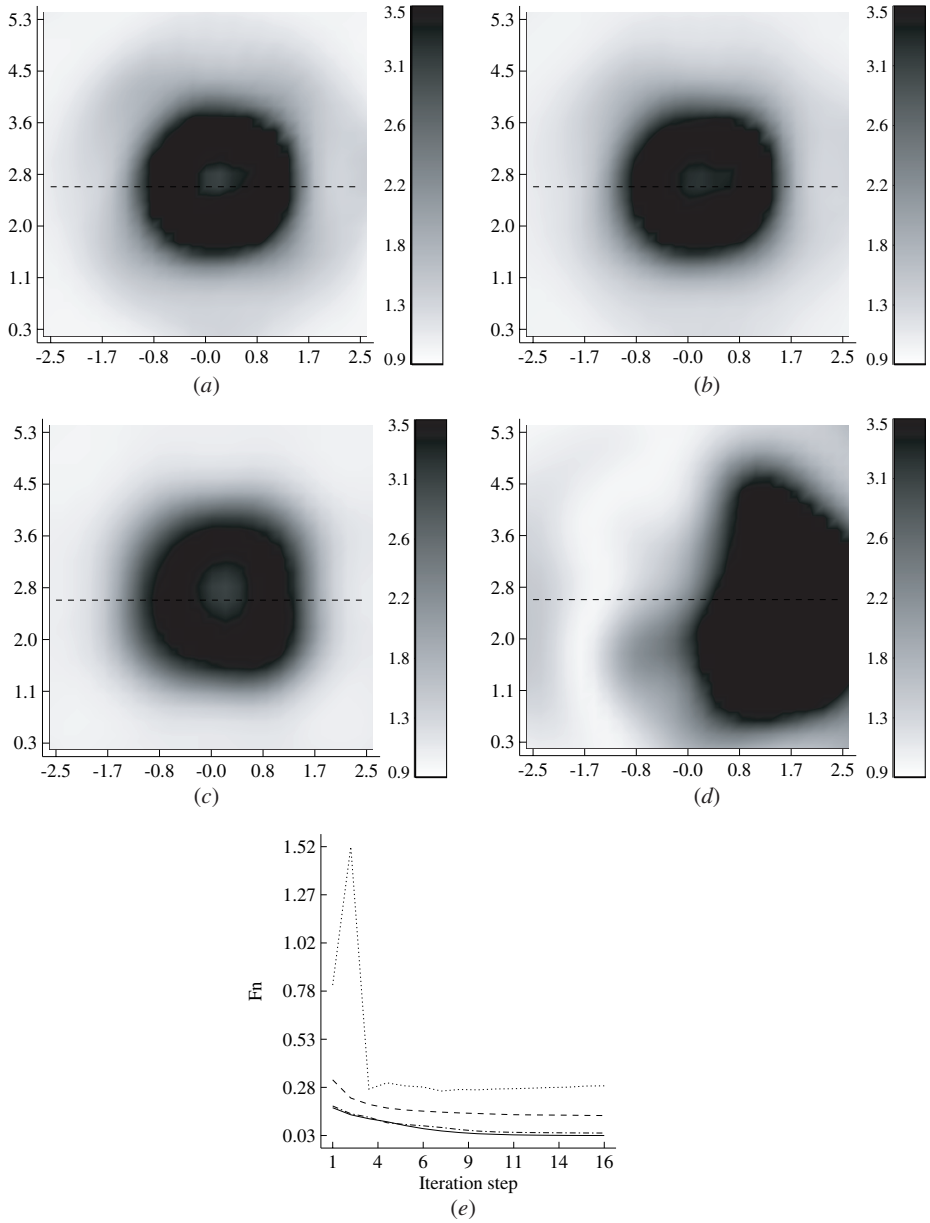

Figure 8. Reconstructed real part of the complex permittivity distribution of the circular dielectric cylinders at $f = 8$ GHz. (*a*) M2GM; (*b*) MGM; (*c*) MBM; (*d*) BM; (*e*) cost function F_n as a function of iteration (——, M2GM; – – –, MGM; — · —, MBM; · · · · · ·, BM). Black in the images represents $\varepsilon_r\,[\cdot] \geqslant 3.5$. Other parameters are specified in the text.

4. Results of inversion from experimental data

All the data were provided courtesy of Institut Fresnel, Marseille, France. The parameters of the experimental setup needed for inversion as well as the database are described in detail in the introduction to the special section. To sum it up briefly, the multiple-frequency data

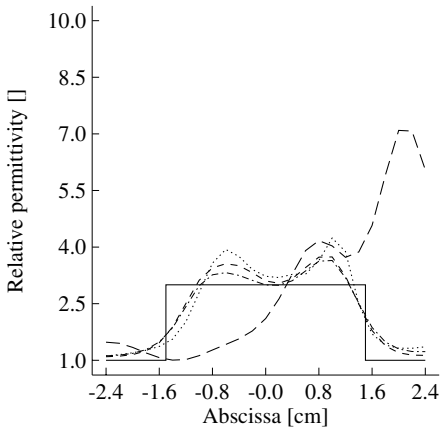

Figure 9. Comparison between the reconstructed profile and the actual one along the diameter plotted in dashed curve in the images of figure 8: ——, actual profile; — · —, M2GM; · · · · · ·, MGM; – – –, MBM; — — —, MB.

correspond to $L = 36$ different source positions evenly distributed along a circle with radius ∼76 cm. The $M = 49$ receivers were also evenly distributed along a circle with radius ∼72 cm with, however, an exclusion area of 120° angular sector. This exclusion area is inherent to the mechanical encumbrance of the experimental setup.

The incident field in Ω used in the inversion (electrically polarized field generated by a line source) was calibrated for each frequency by looking at the measured incident field when the receiving antenna is in front of the emitting one. All the initial guesses are obtained by backpropagation technique and all the reported final results correspond to the 16th iteration. This stopping criterion was motivated firstly by our wish to compare the different methods at the same stage of iteration, and secondly by the need to carry out enough iterations to obtain a significant result. Furthermore, we did not notice any marked changes in the results when continuing iterating. The test domain used in the reconstruction for intermediate and high frequencies was deduced from the result of the inversion at the lowest available frequency, i.e. a large square domain of size (20×20) cm^2 centred at the origin and discretized for numerical purposes into 25×25 square cells. For dielectric targets only the real part of relative permittivity is plotted, while for metallic objects only the conductivity is presented. However, we did not use this *a priori* information in the computation. Yet, in all cases we were able to determine from the low-frequency result if the target under test was dielectric or a highly conducting cylinder.

4.1. Metallic cylinders

Two sets from the database were used to validate our inversion algorithms on metallic targets and we compare the four methods (M2GM, MGM, MBM and BM) at three frequencies: lowest and highest available frequencies plus one intermediate. The first (file name: rectTM_dece.exp) and second (file name: uTM_shaped.exp) set correspond to the off-centred rectangular cylinder and the 'U-shaped' cylinder, respectively.

4.1.1. Rectangular off-centred cylinder. For all methods, from the result at the low frequency $f = 2$ GHz we found that the object falls entirely in a square domain sized (5×5) cm^2 and centred at $y = 4.3$ cm. The maximum value of the reconstructed conductivity is $\sigma = 8.5$, 0.5, 4.6 and 22 S m^{-1} for M2GM, MGM, MBM and BM, respectively. This led to refining the investigating domain Ω for the inversion at higher frequencies, i.e. $f = 4$ and 16 GHz, respectively. Figures 2 and 3 present the results for M2GM, MGM, MBM and BM as well as

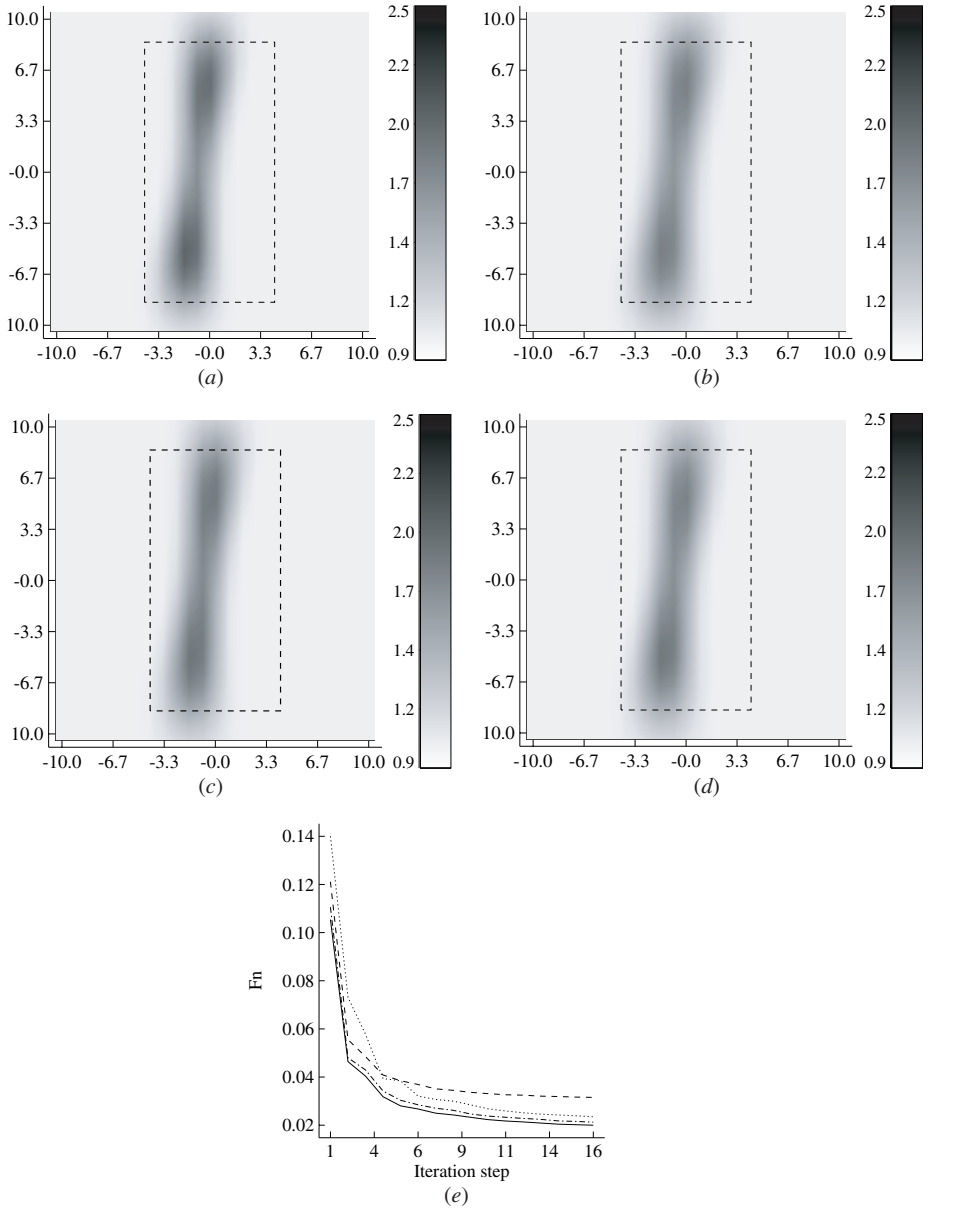

Figure 10. Reconstructed real part of the complex permittivity distribution of two identical circular dielectric cylinders at $f = 1$ GHz. (*a*) M2GM; (*b*) MGM; (*c*) MBM; (*d*) BM; (*e*) cost function F_n as a function of iteration (——, M2GM; – – –, MGM; — · —, MBM; · · · · · ·, BM). The dashed box in the images represents the new test domain Ω used in the inversion at higher frequencies (figures 11 and 13). Other parameters are specified in the text.

the behaviour of the cost functions as a function of the iteration number. Notice that the best result was obtained with M2GM and that for $f = 4$ GHz the cost function does not decrease monotonically for BM, while it does for MBM.

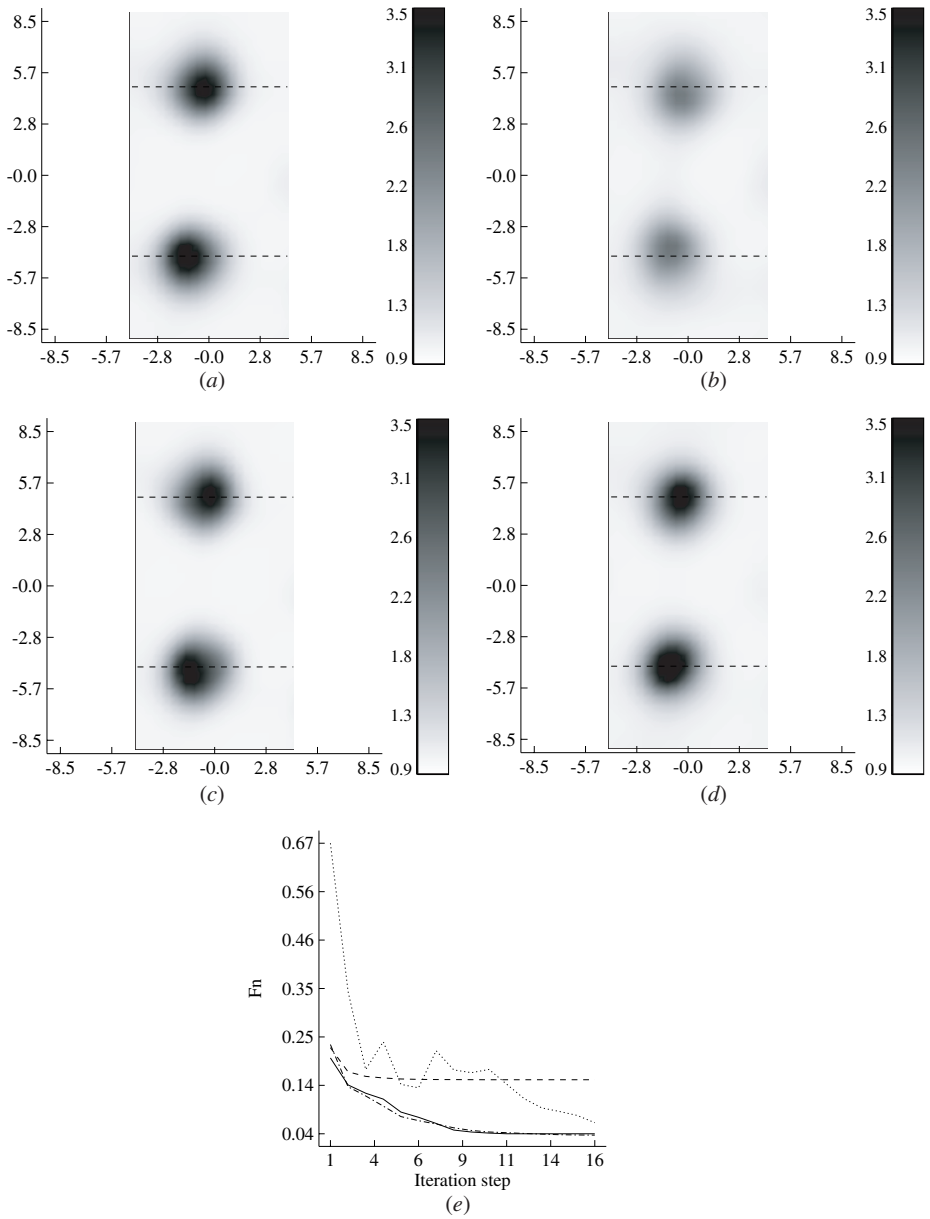

Figure 11. Reconstructed real part of the relative complex permittivity distribution of two identical circular dielectric cylinders at $f = 4$ GHz. (*a*) M2GM; (*b*) MGM; (*c*) MBM; (*d*) MB; (*e*) cost function F_n as a function of iteration (——, M2GM; – – –, MGM; — · —, MBM; · · · · · ·, BM). Other parameters are specified in the text.

4.1.2. 'U-shaped' cylinder. We proceeded the same way as for the rectangular cylinder, i.e. the test domain used in the inversion at higher frequencies ($f = 4$ and 16 GHz) was deduced from the result at the lowest available frequency $f = 2$ GHz. The maximum value of the reconstructed conductivity at $f = 2$ GHz is $\sigma = 2$, 0.6, 0.9 and 1.7 S m^{-1} for M2GM, MGM, MBM and BM, respectively. This new investigating domain Ω consists now in a centred

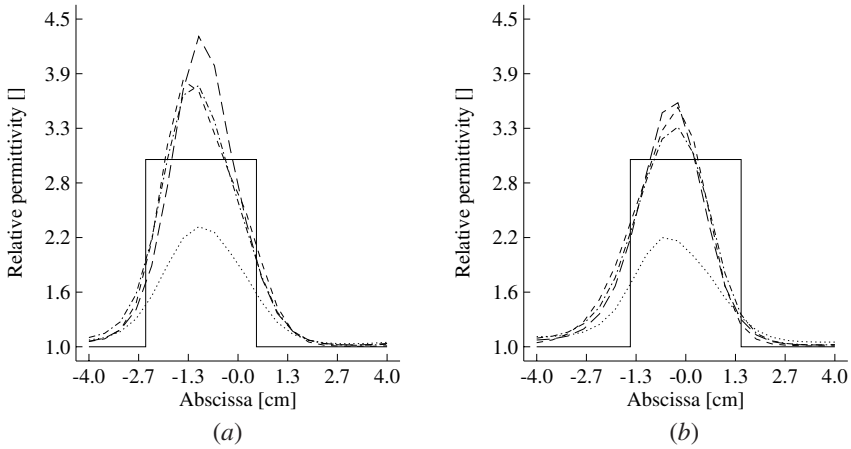

Figure 12. Comparison between the reconstructed profile and the actual one along the diameter plotted in dashed curve in the images of figure 11. (*a*) Lower cylinder (——, actual profile; — · —, M2GM; · · · · · ·, MGM; – – –, MBM; — — —, MB); (*b*) as in (*a*) but for the upper cylinder.

rectangle sized (14×7) cm^2 discretized into 40×20 square cells. Figures 4 and 5 present the final results for all methods at $f = 4$ and 16 GHz, respectively. The results obtained by MGM are deceiving, especially at high frequencies. The artifacts in figures 5 (*a*), (*c*) and (*d*) may be associated with an interior mode of the cavity, since they are separated with respect to the y-axis by approximately $m\,\lambda/2$ with λ being the wavelength in the vacuum and m an integer number.

4.2. Dielectric cylinders

In order to validate our inversion algorithms on dielectric-type targets we used two sets from the database and similarly to metal-type targets we compared the four methods at three frequencies: lowest and highest available frequencies plus one intermediate. The first (file name: dielTM_dec8f.exp) and second (file name: twodielTM_8f.exp) sets correspond to the single off-centred circular dielectric and the two identical circular dielectrics, respectively.

4.2.1. Single off-centred dielectric cylinder. Figures 6–9 present the results of the inversion at $f = 4$ and 8 GHz, respectively. The test domain Ω was deduced from the result at the lowest frequency $f = 1$ GHz. It consists in a square of length 5 cm centred at $y = 2.8$ cm and discretized into 25×25 cells. From figure 6 one can observe that all methods succeeded in localizing the object, but the BM poorly reconstructed both shape and profile (see figure 7) with a chaotic behaviour of the cost function. This is even worse at the highest frequency (see figures 8 and 9).

5. Conclusion

In this paper, we have compared and tested on real data for a wide range of frequencies linearized (BM and MBM), nonlinearized (MGM) and 'hybrid' (M2GM) methods for solving a two-dimensional inverse scattering problem. The results show that M2GM combines the robustness of the MGM with the accuracy (when it converges) of the Born-type methods.

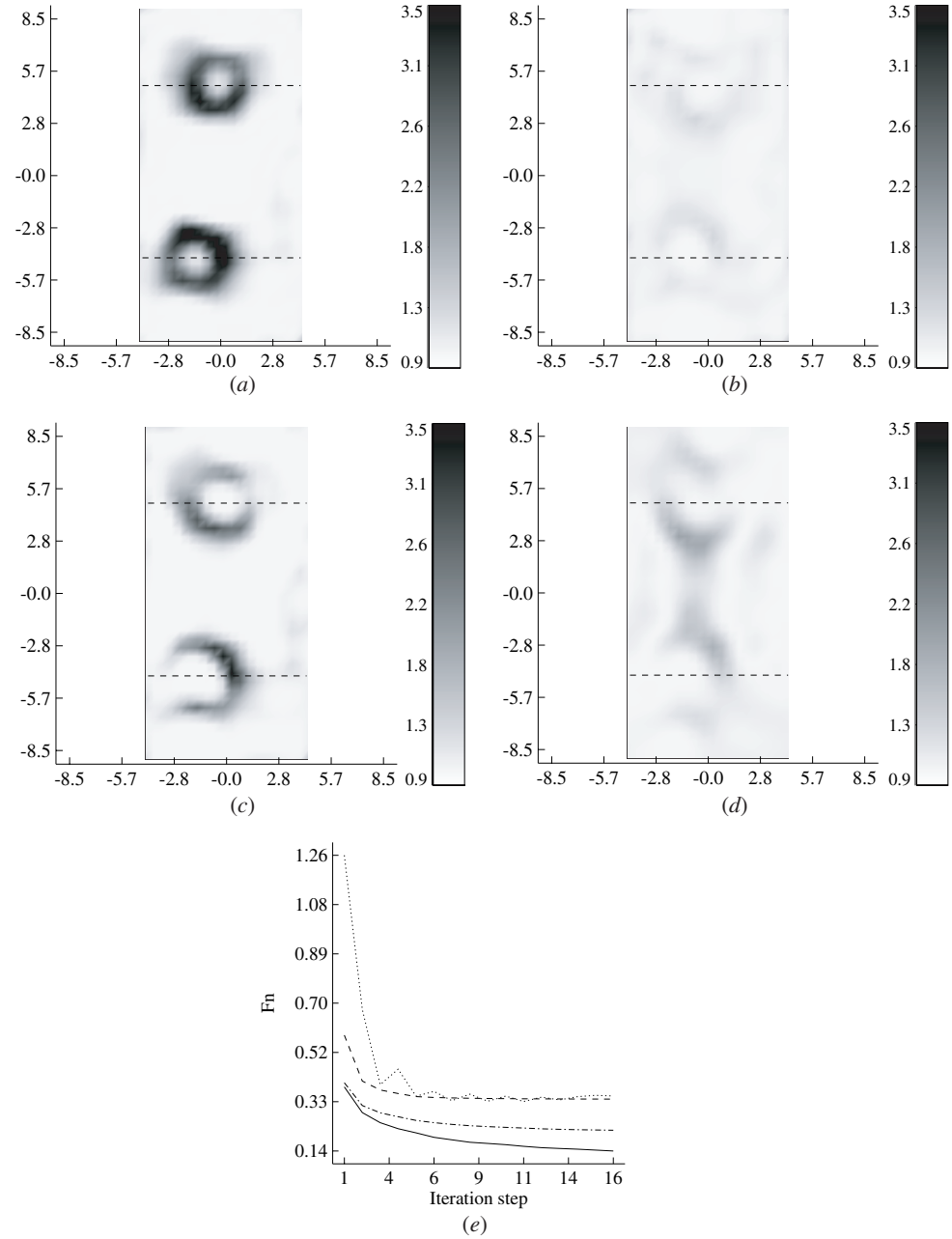

Figure 13. Reconstructed real part of the relative complex permittivity distribution of two identical circular dielectric cylinders at $f = 8$ GHz. (*a*) M2GM; (*b*) MGM; (*c*) MBM; (*d*) MB; (*e*) cost function F_n as a function of iteration (——, M2GM; – – –, MGM; — · —, MBM; · · · · · ·, BM). Other parameters are specified in the text.

Further, it is remarkable that the MBM converges faster than the MGM for all examples. None of the four presented algorithms uses a regularization procedure.

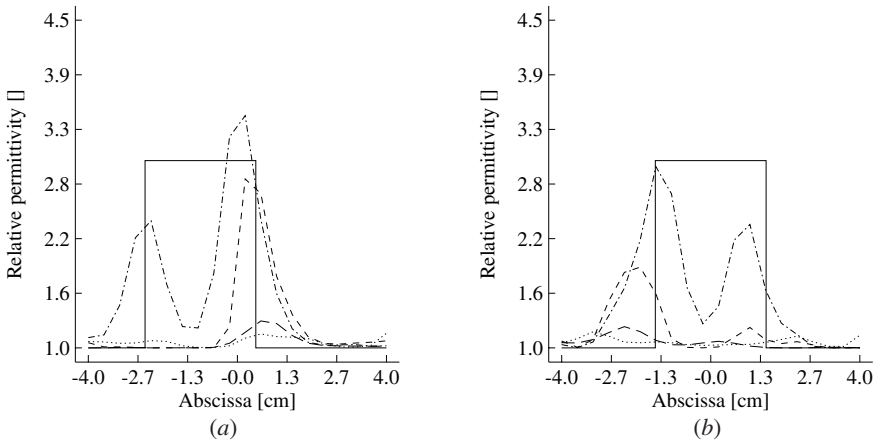

Figure 14. Comparison between the reconstructed profile and the actual one along the diameter plotted in dashed curve in the images of figure 13. (*a*) Lower cylinder (——, actual profile; — · —, M2GM; · · · · · ·, MGM; – – –, MBM; — — —, MB); (*b*) as in (*a*) but for the upper cylinder.

5.1. Two identical dielectric cylinders

Figures 10–14 present the results of the inversion at $f = 1$, 4 and 8 GHz, respectively. The test domain Ω used in the reconstruction presented in figures 11 and 13 consists in a centred rectangle of size (8.5×17) cm^2 and discretized into 20×40 square cells. From figure 10 none of the methods succeeded in detecting the two cylinders and all methods led to more or less the same result. Tuning the frequency from 1 to 4 GHz improved the resolution as one would expect (see figures 11 and 12). For the highest frequency (figure 13), all methods failed with a relative success for M2GM in detecting the two cylinders and retrieving their boundaries (figure 13).

References

[1] Chew W C and Wang Y M 1990 Reconstruction of two-dimensional permittivity distribution using distorted Born iterative method *IEEE Trans. Med. Imaging* **9** 218–25

[2] Joachimowicz N, Pichot C and Hugonin J-P 1991 Inverse scattering: an iterative numerical method for electromagnetic imaging *IEEE Trans. Antennas Propag.* **39** 1742–53

[3] Kleinman R E and van den Berg P M 1992 A modified gradient method for two-dimensional problems in tomography *J. Comput. Appl. Math.* **42** 17–35

[4] Kleinman R E and van den Berg P M 1993 An extended range-modified gradient technique for profile inversion *Radio Sci.* **28** 877–84

[5] Belkebir K, Bonnard S, Pezin F, Sabouroux P and Saillard M 2000 Validation of 2D inverse scattering algorithms from multi-frequency experimental data *J. Electromagn. Waves Appl.* **14** 1637–67

[6] Bonnard S, Saillard M and Vincent P 1999 Improved inverse scattering for dielectric homogeneous cylinders *J. Opt. A: Pure Appl. Opt.* **1** 566–72

[7] van den Berg P M 1999 Reconstruction of media posed as an optimization problem *Wavefield Inversion (CISM Courses and Lectures No 398)* ed A Wirgin (Vienna: Springer) pp 191–240

[8] Souriau L, Duchêne B, Lesselier D and Kleinman R E 1996 Modified gradient approach to inverse scattering for binary objects in stratified media *Inverse Problems* **12** 463–81

[9] Kleinman R E and van den Berg P M 1994 Two-dimensional location and shape reconstruction *Radio Sci.* **29** 1157–69

[10] Belkebir K, Kleinman R E and Pichot C 1997 Microwave imaging—location and shape reconstruction from multifrequency scattering data *IEEE Trans. Microw. Theory Tech.* **45** 469–76

[11] Press W H, Flannery B P, Teukolski S A and Vetterling W T 1986 *Numerical Recipes. The Art of Scientific Computing* (Cambridge: Cambridge University Press)
[12] Peng Z Q and Tijhuis A G 1993 Transient scattering by a lossy dielectric cylinder: marching-on-in-frequency approach *J. Electromagn. Waves Appl.* **7** 739–63